Major modes of climate variability dominate nonlinear Antarctic ice-sheet elevation changes 2002-2020

Matt A. King[1,2], Poul Christoffersen[2,3]

[1]Surveying and Spatial Sciences, School of Geography, Planning, and Spatial Sciences, University of Tasmania, Hobart, Tasmania 7001, Australia

[2]The Australian Centre for Excellence in Antarctic Science, University of Tasmania, Hobart, Tasmania 7001, Australia

[3]Institute for Marine and Antarctic Studies, University of Tasmania, Hobart, Tasmania 7001, Australia

Corresponding author: Matt King (Matt.King@utas.edu.au)

Key Points:

- Cumulative effects of large-scale climate modes dominate detrended altimeter time series of Antarctic ice elevation 2002-2020

- These decadal signals have the same spatial pattern in altimeter ice height and GRACE mass time series.

- These decadal signals are largely due to surface mass balance, but ice dynamic changes may play a role in the Amundsen Sea Embayment

Abstract

19

20 We explore the links between elevation variability of the Antarctic Ice Sheet (AIS) and large-
21 scale climate modes. Using multiple linear regression, we quantify the cumulative effects of El
22 Nino Southern Oscillation (ENSO) and the Southern Annular Mode (SAM) on gridded AIS
23 elevations. Cumulative ENSO and SAM explain a median of 29% of the partial variance and up
24 to 85% in some coastal areas. After spatial smoothing, these signals have high spatial correlation
25 with those from GRACE gravimetry (r~=0.65 each). Much of the signal is removed by a model
26 of firn densification but inter-model differences exist especially for ENSO. At the lower parts of
27 the Thwaites and Pine Island glaciers, near their grounding line, we find the Amundsen Sea Low
28 (ASL) explains ~90% of the observed elevation variability. There, firn effects explain only a
29 small fraction of the variability, suggesting significant height changes have a climatological ice-
30 dynamic response.

31

Plain Language Summary

32

33 This study investigates how variations in the height of the Antarctic Ice Sheet (AIS) are
34 connected to large-scale climate patterns. We used a statistical method to measure the effects of
35 two climate phenomena: El Nino Southern Oscillation (ENSO) and the Southern Annular Mode
36 (SAM). We found that the cumulative effects of these phenomena account for about 29% of the
37 variations in AIS height on average, and up to 85% in some coastal areas. These patterns match
38 well with independent data from the GRACE satellites over the same period. Applying a model
39 that considers the compacting of snow into ice (firn densification) removes much of this signal,
40 suggesting much, but not all, of the signals are related to snowfall variations. At the fronts of the
41 rapidly changing Thwaites and Pine Island glaciers, the dominant climate phenomenon is the
42 Amundsen Sea Low (ASL), which varies in strength and location. Here, the cumulative effects
43 of the ASL changes explain about 90% of the variations in height of these glaciers, with only a
44 small part explained by firn effects. We suggest the unexplained variability is at least partly due
45 to changes in ice flow.

46

1 Introduction

47

48 Observations of the changing volume of the Antarctic Ice Sheet play a major role in
49 understanding ice-sheet change (e.g., Otosaka et al., 2023; Shepherd et al., 2012) from the
50 whole-of-ice-sheet down to individual glaciers (e.g., Smith et al., 2020; Wingham et al., 2009).
51 The now three-decade record of continuous ice volume change captures the variability and
52 longer-term change of both surface mass balance (SMB), and related firn processes, and
53 elevation effects of changing ice dynamics. These changes are, respectively, related to
54 atmospheric and oceanic processes (Horwath et al., 2012; Smith et al., 2020). Several studies
55 have examined the relationship between ice height changes and modes of climate variability, in
56 particular linking them to both El Niño - Southern Oscillation (ENSO) and the Antarctic
57 Circumpolar Wave (Kaitheri et al., 2021; Mémin et al., 2015; Mémin et al., 2014).

58 Strangely, less studied in this context is the role of the dominant mode of climate variability in
59 the Southern Hemisphere, the Southern Annular Mode (SAM). Despite SAM driving variability
60 and trends in SMB across a wide range of timescales (Diener et al., 2021; Medley & Thomas,

61   2019; van den Broeke & van Lipzig, 2017), SAM has yet to be linked to observations of ice
62   sheet elevation change, with one related study reporting no correlation to estimates of ice shelf
63   elevation change (Paolo et al., 2018). By contrast, the cumulative sum of SAM (Diener et al.,
64   2021; Kim et al., 2020) has recently been shown to be linearly related to the dominant signal in
65   detrended surface mass time series derived from satellite gravimetry (King et al., 2023), with
66   large-scale spatially-coherent signal across coastal regions at decadal timescales.

67   The ~300 km spatial resolution of satellite gravimetry, combined with uncertainties in models of
68   SMB (Mottram et al., 2021), meant that King et al. (2023) were not able to separate the relative
69   contributions of SMB and ice dynamical change forced respectively by the atmosphere and
70   ocean (Hansen et al., 2021; Kim et al., 2020; Palóczy et al., 2018; Spence et al., 2017; Thomas et
71   al., 2017; Verfaillie et al., 2022). In particular, ice dynamical change will have a distinct spatial
72   pattern compared to SMB that is not detectable by GRACE but could be possible with altimetry
73   (Smith et al., 2020). Detecting (or otherwise) a response of the grounded ice sheet to large-scale
74   climate variability via the oceans and ice shelves would provide important insights into ice-sheet
75   sensitivity to climate change.

76   In this paper we analyze a recent gridded compilation of satellite altimeter data and compare
77   these time series to cumulative climate indices. We compare the derived signals to those from
78   space gravimetry and then, taking advantage of the high-resolution altimeter data, explore the
79   signal over key ice streams: Thwaites, Pine Island, Totten, and Denman.

80

2 Datasets and Analysis

81

2.1 Altimeter dataset

82

83   We make use of a gridded altimeter product (Nilsson et al., 2023) at 1920 m horizontal
84   resolution and covering the period from Apr 1985 to Dec 2020 (Nilsson et al., 2022). We
85   spatially down-sample this to 5 km horizontal resolution. To facilitate comparison with space
86   gravimetry data we only make use of data from 2002 to the end of the record. The dataset
87   contains monthly ice-sheet elevation-change data derived from a range of radar and laser
88   altimeter missions; over the study period these are ERS-2, Envisat and CryoSat-2 and ICESat
89   and ICESat-2. The approach to accounting for differences in reflection surfaces and other
90   systematic effects is described by Nilsson et al. (2022). To reduce spatial noise we apply a
91   Gaussian smoother with widths specified below, with width defined at the half height of the
92   function, consistent with the definition commonly used in GRACE data smoothing (Wahr et al.,
93   1998).

2.2 Space gravimetry dataset

94

95   We use the COST-G RL01 Level-3 50 km gridded GRACE and GRACE-FO V0002 dataset
96   obtained from http://gravis.gfz-potsdam.de/antarctica (Sasgen et al., 2020). We make use of data
97   from Mar 2002 to Dec 2020, with the end point chosen to match the end of the altimetry dataset.

98 The data are spaced approximately monthly and with a data gap of ~12 months between GRACE
99 and GRACE-FO from mid-2017 to mid-2018.

100 We note that while this product is gridded at 50 km, the intrinsic GRACE resolution is 200-
101 300 km. Post-processing steps include replacement of low-degree GRACE coefficients and
102 insertion of degree-1 terms using standard approaches (Dahle & Murböck, 2020; Sasgen et al.,
103 2020).

104 Since we are interested in decadal variability and trends, we also lightly smooth the altimetry and
105 GRACE data with a Gaussian filter with width 7 months (Wahr et al., 1998).

106 *2.3 Climate indices*

107 We compare the altimeter and GRACE data primarily with SAM and ENSO indices, with
108 additional comparison to Amundsen Sea Low (ASL) indices in the Amundsen Sea region. For
109 the ASL indices, we make use of both the absolute center pressure (ASLP) and longitude (ASLλ)
110 within the ASL Index version 3.20210820-era5 based on monthly ERA5 reanalysis data
111 (Hosking et al., 2016). For SAM, we make use of the Marshall station index (Marshall, 2003).
112 For ENSO, we make use of the Nino3.4 index based on the HadISST1 dataset (Rayner, 2003)
113 and use a 6-month lag (King et al., 2023; Paolo et al., 2018). We normalized each index with the
114 mean and standard deviation computed over 1971-1999 inclusive, then cumulatively summed
115 them, limited them to the data period, and then renormalized to produce SAM_Σ, $ENSO_\Sigma$, $ASLP_\Sigma$,
116 and $ASL\lambda_\Sigma$.

117 The raw indices and their cumulative sums are shown in Fig S1. Correlations above 0.7 are
118 evident between $ASLP_\Sigma$ and SAM_Σ and between $ASL\lambda_\Sigma$ and $ENSO_\Sigma$ (Fig S1, S2). This is due to
119 the ASL being affected by larger-scale modes of climate variability, with SAM in particular
120 modulating its absolute pressure and ENSO modulating the longitude of its center (Clem et al.,
121 2017; Hosking et al., 2016; Turner et al., 2013).

122 *2.4 Multi-variate Empirical Orthogonal Functions*

123 For a data-driven analysis we make use of Multi-variate Empirical Orthogonal Functions
124 (MEOF) (Wang, 1992). MEOFs are an extension of conventional Empirical Orthogonal
125 Functions but allow the dominant modes across multiple variables to be identified rather than
126 treating each variable separately. We use MEOF to analyze the elevation and mass change
127 gridded datasets after individual normalization. We first smooth the altimetry dataset with a
128 50 km-wide Gaussian smoother and sub-sample the altimeter dataset to match the 50 km
129 horizontal resolution of GRACE. Given the limited sampling of altimetry in the northern
130 Antarctic Peninsula we truncate that region from both datasets prior to computing MEOFs.

131 2.5 Regression

132 Using ordinary least squares, we solved the coefficients (*a*, *b*, *c*, *d*, and *e*) of the functional model
133 describing time-evolving elevation (*h*) with time (*t*):
134 $$h(t_i) = a + b(t_i - t_0) + \sum_{k=1}^{2}(c_k^s \sin(2\pi f_k t_i) + c_k^c \cos(2\pi f_k t_i)) + dSAM_\Sigma + eENSO_\Sigma \quad (1)$$

135   Where $f_k = [1, 2]$ cycles per year. We adopted t_0 as the mid point of the altimeter series.

136   2.6 Data uncertainty

137   For regression parameter uncertainties, we recognize the existence of temporal correlations in the
138   altimeter time series (Ferguson et al., 2004), in part due to SMB variation (King & Watson,
139   2020), and take these into account. Following King et al. (2023), we compared trend
140   uncertainties from a linear regression using a Generalized Gauss Markov noise model to those
141   generated using a white noise only (temporally uncorrelated) noise model using HECTOR v2.0
142   software (Bos et al., 2013). For regressions that included the SAM and ENSO terms, the white
143   noise only model produced uncertainties a factor of 3 too small, taken as the median of the ratio
144   of trend uncertainties, or factor 40 too small when not including the SAM and ENSO terms. We
145   applied these scale factors to the uncertainties from the regression. For the GRACE uncertainties
146   we used the scale factors of King et al. (2023).

147   **3 Results**

148   *3.1 Ice-sheet scale analysis*
149   Our data-driven MEOF analysis shows that ice elevation and mass time series are both
150   dominated by decadal-scale variability (Fig. S3c, f). Together, the two leading modes explain
151   65% of the non-linear variance of the combined and smoothed time series. Their corresponding
152   principal components (PCs) correlate with detrended SAM_Σ (r=0.73) and 6-month lagged $ENSO_\Sigma$
153   (r=0.89). The $ASLP_\Sigma$ and $ASL\lambda_\Sigma$ terms are not of direct relevance at the ice-sheet scale given the
154   limited geographical footprint of influence of the ASL, but also have high correlations with the
155   data.
156
157   GRACE and altimetry MEOFs have a high spatial correlation (Fig. S3a-b, d-e; r=0.87 for
158   MEOF1 and r=0.75 for MEOF2) suggesting they are sensing the same signal and are both
159   dominated by coastal changes. The potential in the high-resolution altimetry record is
160   particularly evident in MEOF1 where the spatially-diffuse signal in GRACE (Fig. S3a) is shown
161   to be concentrated over small regions that coincide with the major ice streams of the Amundsen
162   Sea Embayment and the coastline of the Bellingshausen Sea and Marie Byrd Land (Fig. S3b).
163   We note that while MEOF3 (Fig. S4) is partly affected by striping in the GRACE field,
164   characteristic of GRACE systematic error, coherent signal is evident between GRACE and
165   altimetry along the coastlines of the Bellingshausen Sea, Marie Byrd Land and Wilkes Land,
166   suggesting the signal is robust in those regions, although the variance explained (5%) is much
167   smaller than MEOFs 1 and 2. A similar signal to PC3, with periodicities of ~4-7 years, has also
168   been identified in analysis of GRACE data (King et al., 2023; Mémin et al., 2015). Beyond
169   MEOF3, the modes explain little variance (<4%) and are dominated by noise, at least for
170   GRACE (Fig. S4d).
171
172   To quantify the SAM and ENSO contribution to ice sheet elevation change we regress the
173   altimetry time series against SAM_Σ and $ENSO_\Sigma$ and the other parameters in Eq. 1. Here we use
174   the gridded data after applying a 10 km Gaussian spatial filter. The 5 km gridded altimeter
175   regression analysis shown in Fig. 1a,b reveals large-scale spatially coherent signal relating to
176   SAM and ENSO around the coasts of Antarctica. Together, these two terms often explain more
177   than 40% of the partial variance of the timeseries around the coast and into the interior, with the
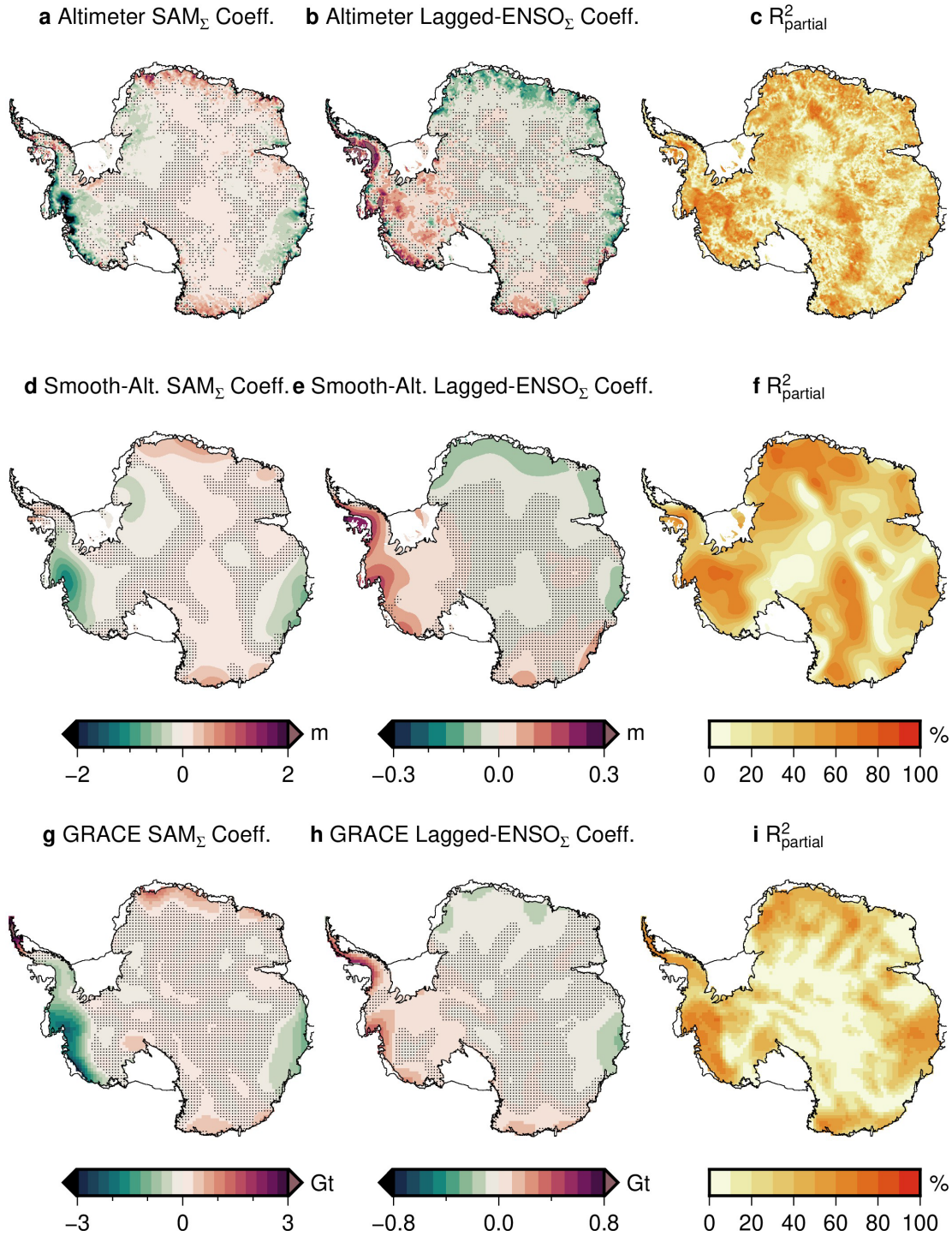
178 partial variance controlling for the other regression terms. The median partial-variance explained
179 across the ice sheet is 29% (Fig. 1c). The SAM_Σ coefficient is strongest in the Amundsen Sea
180 Embayment where it centers on the Pine Island, Thwaites, Smith, and Pope Glaciers (Fig. S5a).
181 The negative elevation signal in this region is linked to periods where positive SAM dominates
182 negative SAM (positive SAM_Σ). Other strong signal exists along the coastal zone of the
183 Bellingshausen Sea, Marie Byrd Land, and parts of coastal East Antarctica. A more diffuse
184 signal is evident in the interior of West Antarctica and parts of East Antarctica (Fig. S6a). The
185 $ENSO_\Sigma$ coefficient has particularly high positive values, indicating elevation increase associated
186 with sustained El Niño, along the coast of the Bellingshausen Sea and well upstream into Pine
187 Island Glacier (Fig. S5b)
188
189 Applying a 200 km Gaussian smoother to the altimeter data and rerunning the regression (Fig.
190 1d-e) produces coefficients with large-scale spatial coherence and larger partial variances
191 explained, often exceeding 60% in key coastal regions but extending well into the interior of the
192 ice sheet (Fig. 1f). Comparing them to results of a regression with GRACE data (Fig. 1g-h)
193 (King et al., 2023) shows high agreement in the signs and spatial distribution of the signal. We
194 note that there are insufficient altimeter data in the Northern Antarctic Peninsula to analyze the
195 signal in this region. Computing spatial correlations between the smoothed altimetry regression
196 and the GRACE regression gives r=0.65 for SAM_Σ and r=0.68 for $ENSO_\Sigma$.
197
198 We next examine the role of SMB variability on the estimated coefficients from the altimetry
199 regression. To do this we subtract the IMAU Firn Densification Model (IMAU FDM) v1.2A
200 (Veldhuijsen et al., 2023) from the altimetry time series and repeat the regression. The results are
201 shown in Figure 2. Comparing Fig. 2a with Fig. 1a shows that IMAU FDM effectively removes
202 all the SAM-related signal in East Antarctic Ice Sheet (EAIS) but much of the SAM signal
203 remains in West Antarctic Ice Sheet (WAIS). Much of the coastal EAIS ENSO-related signal is
204 removed by IMAU FDM but with small over-correction evident for much of the ice sheet,
205 including signal reversing sign in George V Land and WAIS. Repeating the regression but
206 instead using the GSFC FDM v1.2.1 (Medley et al., 2022) shows that there is significant
207 sensitivity to the choice of FDM (Fig. 2d-f), with GSFC FDM apparently over-correcting ENSO-
208 related signal in the Totten Glacier region but in much better agreement with the altimetry in
209 WAIS. Given the decadal timescales of the signals, these inter-model differences are likely to
210 have contributions from both the FDMs themselves and their underlying SMB models (Medley
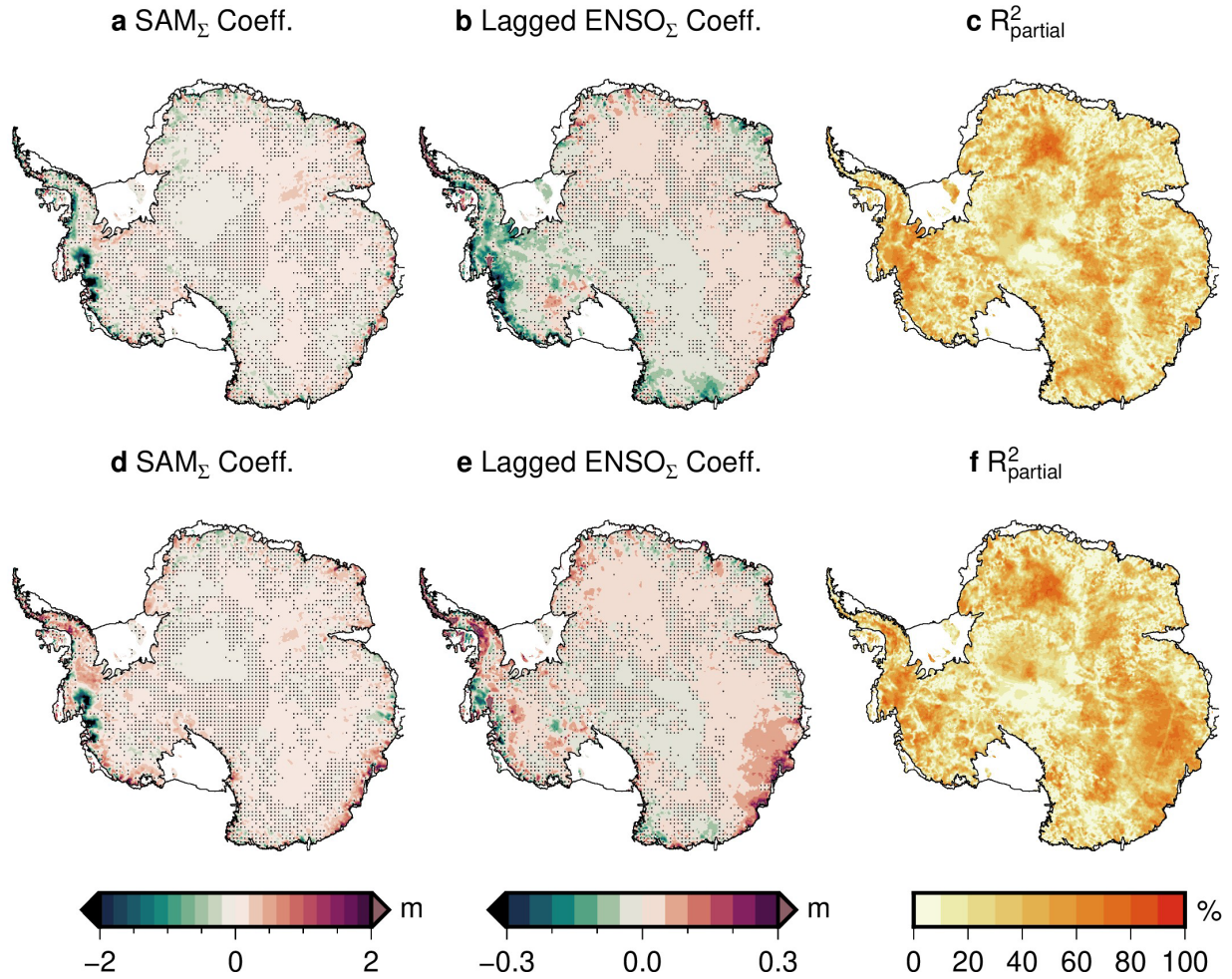211 et al., 2022).
212
213 The combination of coefficients estimated from each of GRACE and altimetry allows the density
214 of these terms to be estimated. Given the GRACE resolution half-width is about 100km, we
215 computed densities and their at locations 100 km upstream of the grounding lines of the
216 Thwaites, Pine Island, Totten, and Denman glacier. These computed densities are sensitive to the
217 radius of the Gaussian smoother applied to the altimetry data, and we adopted a 200 km
218 smoother to approximate the GRACE resolution. ENSO-related results are highly uncertain in
219 the Denman and Totten glacier regions due to limited signal, but the other densities (SAM and
220 ENSO related) suggest the observed changes have a density between snow and ice, clustering
221 around 600 kg/m^3 (Fig. S6). While the estimates are uncertain, they suggest that some of the
222 signal could originate in ice dynamics rather than SMB.

223

a Altimeter SAM$_\Sigma$ Coeff. **b** Altimeter Lagged-ENSO$_\Sigma$ Coeff. **c** R$^2_{partial}$

d Smooth-Alt. SAM$_\Sigma$ Coeff. **e** Smooth-Alt. Lagged-ENSO$_\Sigma$ Coeff. **f** R$^2_{partial}$

g GRACE SAM$_\Sigma$ Coeff. **h** GRACE Lagged-ENSO$_\Sigma$ Coeff. **i** R$^2_{partial}$

224

Figure 1. Results of regression analysis of gridded data. Shown are the SAM$_\Sigma$ and ENSO$_\Sigma$
coefficients and variances explained for the altimetry (top row), altimetry after 200 km Gaussian
smoothing (middle row), and GRACE (bottom row). The partial variances explained by SAM$_\Sigma$
and lagged ENSO$_\Sigma$ are in the right column.

229

230

Figure 2. Results of regression analysis of FDM-corrected gridded altimeter data. Regression coefficients are shown (left and central columns) and the partial variances explained by SAM_Σ and lagged $ENSO_\Sigma$ (right column). Shown are the coefficients and variances explained for the altimetry time series after subtracting of the IMAU FDM (top row) and GSFC FDM (bottom row).

237

Next, we explore the origins of these signals further on a glacier-by-glacier basis.

239

3.2 Regional scale analysis

3.2.1 Thwaites and Pine Island glaciers

The partial variance explained by the SAM_Σ and $ENSO_\Sigma$ terms (before subtracting an FDM) is above 60% for much of the Amundsen Sea Embayment (ASE; Fig. 1c, f; S5c,f). Regardless of the FDM model adopted, much SAM_Σ signal remains in the ASE broadly and $ENSO_\Sigma$ signal is evident in the Pine Island Glacier region (Fig. 2). Closer examination of these regions in Fig. S5

246 (top row) indicates that the ASE signals are concentrated along low-elevation and fast flowing
247 regions that correspond to Pine Island, Thwaites, and nearby glaciers. This is further evidenced
248 through cross-sections near to the front of these glaciers (Fig. S7) along the yellow lines in Fig
249 S5. It is notable that the phase of the SAM-related signal is switched in the fast-flowing region of
250 Pine Island Glacier.

251 Coefficient magnitudes generally decay upstream of the grounding line (Fig. S8). Subtracting the
252 IMAU FDM before performing the regression results in coefficients along the centerline and
253 cross profiles that are shifted nearly uniformly but are not significantly altered in their spatial
254 pattern (dashed lines Fig. S7-S8). Together these results suggest there may be an ice dynamic
255 component within the SAM_Σ and $ENSO_\Sigma$ coefficients in addition to residual SMB/FDM signal.
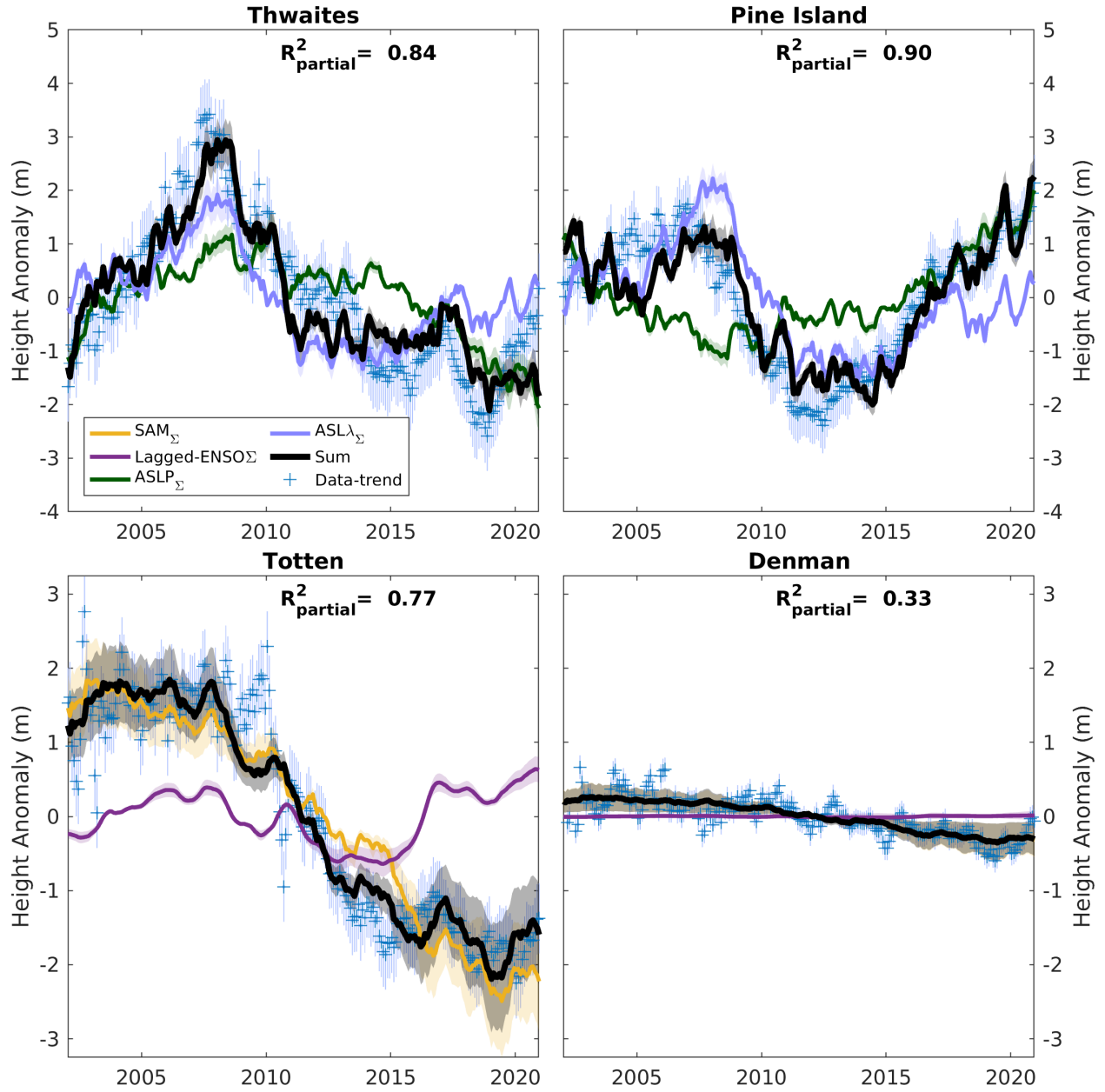
256 Along the coastal margin of the ASE the climatology is more directly controlled by the ASL than
257 SAM and ENSO which modulate its depth and location (Clem et al., 2017; Turner et al., 2013).
258 To explore this further we repeated the regression replacing SAM_Σ and $ENSO_\Sigma$ in Equation 1
259 with $ASLP_\Sigma$ and $ASL\lambda_\Sigma$. While the magnitude of the estimated coefficients differs between
260 SAM_Σ/-$ASLP_\Sigma$ and $ENSO_\Sigma$/-$ASL\lambda_\Sigma$ the broader spatial pattern will be nearly identical due to the
261 high correlations of these coefficient pairs over the data period (Fig. S1-S2) and so we just
262 explore in detail the impact of estimating the ASL coefficients at one point location per glacier,
263 at a centerline location about 20 km upstream of their respective grounding lines (Fig. S5 yellow
264 crosses; Table S1).

265 The detrended data are shown in Fig. 3 (top row) where they reveal non-linear variability of
266 several meters over the data period (blue plusses). Time series of estimated ASL coefficients
267 sum to closely reproduce the data (black line). These two terms explain 84% (Thwaites) and 90%
268 (Pine Island) of the partial variance of the altimeter time series. Interestingly, the phase of the
269 $ASLP_\Sigma$ term is opposite between Thwaites and Pine Island, while the $ASL\lambda_\Sigma$ term is in phase.

270 Neither of the FDM models can explain the elevation variability at Thwaites or Pine Island
271 glaciers (Fig. S9, brown lines). This could be because the SMB models are unable to reproduce
272 the precipitation in this region, especially in ~2007 at Thwaites Glacier, but this would require a
273 highly localized signal as this event does not occur at Pine Island Glacier. The misfit could be
274 caused by errors in background altimeter models, however we note we obtain nearly identical
275 results using the alternative dataset of Schröder et al. (2019). The most likely source of the
276 unexplained height signal is ice flow dynamics responding to large-scale climate variability.
277
278 The dynamic effect of ice flow and its influence on ice sheet mass and surface elevation at a
279 given point can be estimated from satellite-derived glacier velocities and the principle of mass
280 conservation (Supplementary Text S1). Based on year-on-year changes in ice velocity since
281 2003, it is reasonable to expect several meters of dynamic elevation change in the lower parts of
282 Pine Island and Thwaites due to a combination of advection and strain thinning (Fig. S10).

283

Figure 3. Detrended elevation time series at glacier point locations. Time series are shown for sites ~20 km upstream of the grounding line and along the centerline of flow (Fig. S5 yellow crosses; Table S1). Shown are the altimeter time series after 10 km Gaussian smoothing and subtracting the estimated trend and harmonics (blue plusses), and the two components of the model (colored lines) and their sum (black line) for each glacier. For Thwaites and Pine Island glaciers (top row), ASL coefficients are shown, while for Totten and Denman glaciers (bottom row) SAM and ENSO terms are shown. The partial variances explained by the sum of the two coefficients are listed in each panel. Grey shading is the 1-sigma uncertainty of the model. Error bars represent the 2-sigma uncertainties of the data.

295   3.2.2 Totten and Denman glaciers

296   The SAM and ENSO coefficients in the region of Totten and Denman glaciers have smaller
297   magnitude and are much more diffuse than in the ASE (Fig. S5d-e). Nonetheless, these terms
298   explain significant amounts of the partial variance (Fig. S5f) in this region. There is almost no
299   non-linear signal to explain near the front of the Denman Glacier (Fig. 3), with the largest SAM
300   or ENSO signal in the Denman region is west of Denman. Nonetheless, SAM contributes about
301   30% of the partial variance at Denman. If the underlying surface lowering trend of Denman is
302   affected by climate variability it is not obviously associated with SAM and ENSO over this
303   period.

304   Despite the modest signal near Totten there is still evidence that significant SAM and ENSO
305   signals exist in the fast-flowing region of Totten Glacier (Fig. 3), at least in the 20-30 km above
306   the grounding zone (Fig. S7c, Fig. S8). Unlike the ASE glaciers, there is insufficient ice velocity
307   time series for Totten Glacier to explore the cumulative impacts of time-varying ice dynamics on
308   ice elevation. As noted above, the FDM-corrected results are model-dependent in this region and
309   so the origin(s) of the Totten Glacier non-linear elevation change signal is unclear but may
310   contain a component due to ice dynamic changes.

311   **4 Discussion**

312   Our analysis reveals the spatial fingerprints of SAM and ENSO on AIS elevation over 2002-
313   2021, patterns which are confirmed by analysis of GRACE mass change data over the same
314   period. These patterns may not be stationary with time. Indeed, circulation patterns associated
315   with SAM are known to vary over decades (Marshall et al., 2013; Silvestri & Vera, 2009), with
316   effects including variable precipitation in the Antarctic Peninsula (Goodwin et al., 2016). Within
317   this context it is therefore not unexpected that our pattern of SAM variability is different to the
318   SMB-only SAM reconstruction of Medley and Thomas (2019) for the second half of the 20th
319   century for instance. Differences with SMB-only reconstructions would also result if ice-
320   dynamic effects on ice elevation and mass were non-negligible as hinted at by our data.
321
322   There are only a few previous studies exploring the relationship between ice dynamics,
323   expressed as changes in ice mass, thickness, or elevation, and modes of climate variability, most
324   notably in the Amundsen Sea Embayment region (Christie et al., 2023). In particular, Dutrieux et
325   al. (2014) found reduced PIG ice shelf melt during a strong 2012 La Niña. Consistent with this,
326   Paolo et al. (2018) found PIG ice shelf melting increased during El Niño, reducing ice shelf
327   thickness, but that the ice shelf elevation increased overall due to increased accumulation. Our
328   finding that PIG increases in elevation upstream of its grounding line when El Niño is sustained
329   (or sustained westward ASL position), while the glacier is also dynamically thinning (Fig. S10),
330   is consistent with this overall picture.
331
332   The SAM/ASLP-related signal upstream of PIG, Thwaites, and other ASE glaciers is the largest
333   unexplained signal in Antarctica. The spatial pattern, with largest signal at lowest elevations,
334   could be explained by both ice dynamics or unmodeled SMB or firn densification. Limited
335   idealized study of the impacts of SAM on ASE basal melt is consistent with our observation of
336   reduced upstream elevation with positive SAM but with melt response times that are decades
337   longer than our analysis explores (Verfaillie et al., 2022), perhaps ruling out SAM but leaving
338   the possibility of the localized ASLP as a source of immediate changes in buttressing.

339

340   We note that while the SAM_Σ and $ASLP_\Sigma$ signals are correlated and our analysis cannot separate
341   their different effects, they have different long-term implications for the ice sheet. As discussed
342   by King et al. (2023), SAM_Σ has a trend due to the positive phase of SAM that has emerged since
343   the 1940s. $ASLP_\Sigma$ does not have a strong long-term trend, and so the extent to which the changes
344   in coastal West Antarctica are related to the ASL rather than SAM will reduce the inferred
345   contribution of SAM to ice-mass loss over recent decades (King et al., 2023).

346

347   Finally, our findings offer a simple way to remove decadal-scale variability from altimetry time
348   series. This reduces correlated noise in the time series and will alter both the derived trends and,
349   perhaps most significantly, the uncertainties of derived trends and other parameters if correlated
350   noise is considered in the regression as it should (Ferguson et al., 2004; King & Watson, 2020;
351   Williams et al., 2014; Wouters et al., 2013).

352

5 Conclusions

354   We analyzed gridded Antarctic ice elevation time series and show that much of the time series
355   variance can be explained through a simple linear model based on the cumulative indices of the
356   Southern Annular Mode and El Nino Southern Oscillation. The spatial pattern of this signal,
357   once spatially smoothed, is in close agreement with the spatial pattern evident in GRACE data
358   suggesting that observed ice elevation variability is robust and climatological. The Amundsen
359   Sea Low is more directly relevant to the Amundsen Sea Embayment and we show that variations
360   in its pressure and longitude explain ~90% of the variance over Pine Island and Thwaites
361   glaciers.

362   Subtracting the effects of modeled firn densification removes much, but not all, signal, with
363   inter-model differences evident. Residual climatological signal is particularly large at the fronts
364   of fast-flowing glaciers in the Amundsen Sea Embayment. We suggest that ice dynamic effects
365   may be contributing to this signal. Computing changes in elevation due to observed variation in
366   horizontal velocity suggests the velocities are potential of the right magnitude to explain it.
367   Further work is required to quantify the magnitude and response-times of upstream ice to
368   changes in climatological variability in ice shelf melt.

369

374

Open Research

Data Availability Statement

All underlying data are openly available. Altimetry data were obtained from
https://doi.org/10.5067/L3LSVDZS15ZV . GRACE time series were obtained from
http://gravis.gfz-potsdam.de/ais . The IMAU FDM was obtained from
https://doi.org/10.5281/zenodo.5172513 . The GSFC FDM was obtained from
https://zenodo.org/record/7054574#.Y0iiTnbMJPY . SAM index time series were obtained from
http://www.nerc-bas.ac.uk/public/icd/gjma/newsam.1957.2007.txt . ASL data were obtained
from https://scotthosking.com/asl_index using version 3.20210820-era5. Nino3.4 index time
series were obtained from
https://psl.noaa.gov/gcos_wgsp/Timeseries/Data/nino34.long.anom.data . ==Data presented here
will be made openly available upon acceptance==.

References

Bos, M. S., Fernandes, R. M. S., Williams, S. D. P., & Bastos, L. (2013). Fast error analysis of continuous GNSS observations with missing data. *Journal of Geodesy, 87*(4), 351-360. doi:10.1007/s00190-012-0605-0

Christie, F. D. W., Steig, E. J., Gourmelen, N., Tett, S. F. B., & Bingham, R. G. (2023). Inter-decadal climate variability induces differential ice response along Pacific-facing West Antarctica. *Nature Communications, 14*(1), 93. doi:10.1038/s41467-022-35471-3

Clem, K. R., Renwick, J. A., & McGregor, J. (2017). Large-Scale Forcing of the Amundsen Sea Low and Its Influence on Sea Ice and West Antarctic Temperature. *Journal of Climate, 30*(20), 8405-8424. doi:10.1175/Jcli-D-16-0891.1

Dahle, C., & Murböck, M. (2020). *Post-processed GRACE/GRACE-FO Geopotential GSM Coefficients COST-G RL01 (Level-2B Product)*. doi:10.5880/GFZ.GRAVIS_06_L2B

Diener, T., Sasgen, I., Agosta, C., Fürst, J. J., Braun, M. H., Konrad, H., & Fettweis, X. (2021). Acceleration of Dynamic Ice Loss in Antarctica From Satellite Gravimetry. *Frontiers in Earth Science, 9*. Original Research. doi:10.3389/feart.2021.741789

Dutrieux, P., De Rydt, J., Jenkins, A., Holland, P. R., Ha, H. K., Lee, S. H., et al. (2014). Strong Sensitivity of Pine Island Ice-Shelf Melting to Climatic Variability. *Science, 343*(6167), 174-178. doi:doi:10.1126/science.1244341

Ferguson, A. C., Davis, C. H., & Cavanaugh, J. E. (2004). An autoregressive model for analysis of ice sheet elevation change time series. *Ieee Transactions on Geoscience and Remote Sensing, 42*(11), 2426-2436. Article. doi:10.1109/tgrs.2004.836788

Goodwin, B. P., Mosley-Thompson, E., Wilson, A. B., Porter, S. E., & Sierra-Hernandez, M. R. (2016). Accumulation Variability in the Antarctic Peninsula: The Role of Large-Scale Atmospheric Oscillations and Their Interactions. *Journal of Climate, 29*(7), 2579-2596. doi:10.1175/JCLI-D-15-0354.1

Hansen, N., Langen, P. L., Boberg, F., Forsberg, R., Simonsen, S. B., Thejll, P., et al. (2021). Downscaled surface mass balance in Antarctica: impacts of subsurface processes and large-scale atmospheric circulation. *The Cryosphere, 15*(9), 4315-4333. doi:10.5194/tc-15-4315-2021

Horwath, M., Legresy, B., Remy, F., Blarel, F., & Lemoine, J. M. (2012). Consistent patterns of Antarctic ice sheet interannual variations from ENVISAT radar altimetry and GRACE satellite gravimetry. *Geophysical Journal International, 189*(2), 863-876. doi:10.1111/j.1365-246X.2012.05401.x

Hosking, J. S., Orr, A., Bracegirdle, T. J., & Turner, J. (2016). Future circulation changes off West Antarctica: Sensitivity of the Amundsen Sea Low to projected anthropogenic forcing. *Geophysical Research Letters, 43*(1), 367-376. doi:10.1002/2015GL067143

Kaitheri, A., Mémin, A., & Rémy, F. (2021). Inter-Annual Variability in the Antarctic Ice Sheets Using Geodetic Observations and a Climate Model. *Remote Sensing, 13*(11), 2199.

Kim, B.-H., Seo, K.-W., Eom, J., Chen, J., & Wilson, C. R. (2020). Antarctic ice mass variations from 1979 to 2017 driven by anomalous precipitation accumulation. *Scientific Reports, 10*(1), 20366. doi:10.1038/s41598-020-77403-5

King, M. A., Lyu, K., & Zhang, X. (2023). Climate variability a key driver of recent Antarctic ice-mass change. *Nature Geoscience, 16*(12), 1128-1135. doi:10.1038/s41561-023-01317-w

King, M. A., & Watson, C. S. (2020). Antarctic Surface Mass Balance: Natural Variability, Noise, and Detecting New Trends. *Geophysical Research Letters, 47*(12), e2020GL087493. doi:10.1029/2020GL087493

Marshall, G. J. (2003). Trends in the Southern Annular Mode from Observations and Reanalyses. *Journal of Climate, 16*(24), 4134-4143. doi:10.1175/1520-0442(2003)016<4134:Titsam>2.0.Co;2

Marshall, G. J., Orr, A., & Turner, J. (2013). A Predominant Reversal in the Relationship between the SAM and East Antarctic Temperatures during the Twenty-First Century. *Journal of Climate, 26*(14), 5196-5204. doi:10.1175/Jcli-D-12-00671.1

Medley, B., Neumann, T. A., Zwally, H. J., Smith, B. E., & Stevens, C. M. (2022). Simulations of firn processes over the Greenland and Antarctic ice sheets: 1980–2021. *The Cryosphere, 16*(10), 3971-4011. doi:10.5194/tc-16-3971-2022

Medley, B., & Thomas, E. R. (2019). Increased snowfall over the Antarctic Ice Sheet mitigated twentieth-century sea-level rise. *Nature Climate Change, 9*(1), 34-39. doi:10.1038/s41558-018-0356-x

Mémin, A., Flament, T., Alizier, B., Watson, C., & Rémy, F. (2015). Interannual variation of the Antarctic Ice Sheet from a combined analysis of satellite gravimetry and altimetry data. *Earth and Planetary Science Letters, 422*(0), 150-156. doi:10.1016/j.epsl.2015.03.045

Mémin, A., Flament, T., Rémy, F., & Llubes, M. (2014). Snow- and ice-height change in Antarctica from satellite gravimetry and altimetry data. *Earth and Planetary Science Letters, 404*(0), 344-353. doi:10.1016/j.epsl.2014.08.008

Mottram, R., Hansen, N., Kittel, C., van Wessem, J. M., Agosta, C., Amory, C., et al. (2021). What is the surface mass balance of Antarctica? An intercomparison of regional climate model estimates. *The Cryosphere, 15*(8), 3751-3784. doi:10.5194/tc-15-3751-2021

Nilsson, J., Gardner, A., & Paolo, a. F. S. (2023). *MEaSUREs ITS_LIVE Antarctic Grounded Ice Sheet Elevation Change, Version 1*. Retrieved from: https://nsidc.org/data/NSIDC-0782/versions/1 doi:10.5067/L3LSVDZS15ZV

Nilsson, J., Gardner, A. S., & Paolo, F. S. (2022). Elevation change of the Antarctic Ice Sheet: 1985 to 2020. *Earth Syst. Sci. Data, 14*(8), 3573-3598. doi:10.5194/essd-14-3573-2022

Otosaka, I. N., Shepherd, A., Ivins, E. R., Schlegel, N. J., Amory, C., van den Broeke, M. R., et al. (2023). Mass balance of the Greenland and Antarctic ice sheets from 1992 to 2020. *Earth Syst. Sci. Data, 15*(4), 1597-1616. doi:10.5194/essd-15-1597-2023

Palóczy, A., Gille, S. T., & McClean, J. L. (2018). Oceanic Heat Delivery to the Antarctic Continental Shelf: Large-Scale, Low-Frequency Variability. *Journal of Geophysical Research: Oceans, 123*(11), 7678-7701. doi:10.1029/2018JC014345

Paolo, F. S., Padman, L., Fricker, H. A., Adusumilli, S., Howard, S., & Siegfried, M. R. (2018). Response of Pacific-sector Antarctic ice shelves to the El Niño/Southern Oscillation. *Nature Geoscience, 11*(2), 121-126. doi:10.1038/s41561-017-0033-0

Rayner, N. A. (2003). Global analyses of sea surface temperature, sea ice, and night marine air temperature since the late nineteenth century. *Journal of Geophysical Research, 108*(D14). doi:10.1029/2002jd002670

Sasgen, I., Groh, A., & Horwath, M. (2020). *COST-G GravIS RL01 Ice-Mass Change Products*. doi:10.5880/COST-G.GRAVIS_01_L3_ICE

Schröder, L., Horwath, M., Dietrich, R., Helm, V., van den Broeke, M. R., & Ligtenberg, S. R. M. (2019). Four decades of Antarctic surface elevation changes from multi-mission satellite altimetry. *The Cryosphere, 13*(2), 427-449. doi:10.5194/tc-13-427-2019

Shepherd, A., Ivins, E. R., A, G., Barletta, V. R., Bentley, M. J., Bettadpur, S., et al. (2012). A Reconciled Estimate of Ice-Sheet Mass Balance. *Science, 338*(6111), 1183-1189. doi:10.1126/science.1228102

Silvestri, G., & Vera, C. (2009). Nonstationary Impacts of the Southern Annular Mode on Southern Hemisphere Climate. *Journal of Climate, 22*(22), 6142-6148. doi:10.1175/2009JCLI3036.1

Smith, B., Fricker, H. A., Gardner, A. S., Medley, B., Nilsson, J., Paolo, F. S., et al. (2020). Pervasive ice sheet mass loss reflects competing ocean and atmosphere processes. *Science, 368*(6496), 1239-1242. doi:doi:10.1126/science.aaz5845

477 Spence, P., Holmes, R. M., Hogg, A. M., Griffies, S. M., Stewart, K. D., & England, M. H. (2017). Localized rapid
478   warming of West Antarctic subsurface waters by remote winds. *Nature Climate Change, 7*(8), 595-603.
479   doi:10.1038/nclimate3335
480 Thomas, E. R., van Wessem, J. M., Roberts, J., Isaksson, E., Schlosser, E., Fudge, T. J., et al. (2017). Regional
481   Antarctic snow accumulation over the past 1000 years. *Clim. Past, 13*(11), 1491-1513. doi:10.5194/cp-13-
482   1491-2017
483 Turner, J., Phillips, T., Hosking, J. S., Marshall, G. J., & Orr, A. (2013). The Amundsen Sea low. *International
484   Journal of Climatology, 33*(7), 1818-1829. doi:10.1002/joc.3558
485 van den Broeke, M. R., & van Lipzig, N. P. M. (2017). Changes in Antarctic temperature, wind and precipitation in
486   response to the Antarctic Oscillation. *Annals of Glaciology, 39*, 119-126.
487   doi:10.3189/172756404781814654
488 Veldhuijsen, S. B. M., van de Berg, W. J., Brils, M., Kuipers Munneke, P., & van den Broeke, M. R. (2023).
489   Characteristics of the 1979–2020 Antarctic firn layer simulated with IMAU-FDM v1.2A. *The Cryosphere,
490   17*(4), 1675-1696. doi:10.5194/tc-17-1675-2023
491 Verfaillie, D., Pelletier, C., Goosse, H., Jourdain, N. C., Bull, C. Y. S., Dalaiden, Q., et al. (2022). The circum-
492   Antarctic ice-shelves respond to a more positive Southern Annular Mode with regionally varied melting.
493   *Communications Earth & Environment, 3*(1), 139. doi:10.1038/s43247-022-00458-x
494 Wahr, J., Molenaar, M., & Bryan, F. (1998). Time variability of the Earth's gravity field: Hydrological and oceanic
495   effects and their possible detection using GRACE. *Journal of Geophysical Research: Solid Earth,
496   103*(B12), 30205-30229. doi:10.1029/98JB02844
497 Wang, B. (1992). The Vertical Structure and Development of the Enso Anomaly Mode during 1979-1989. *Journal
498   of the Atmospheric Sciences, 49*(8), 698-712. doi:10.1175/1520-0469(1992)049<0698:Tvsado>2.0.Co;2
499 Williams, S. D. P., Moore, P., King, M. A., & Whitehouse, P. L. (2014). Revisiting GRACE Antarctic ice mass
500   trends and accelerations considering autocorrelation. *Earth and Planetary Science Letters, 385*, 12-21.
501   doi:10.1016/j.epsl.2013.10.016
502 Wingham, D. J., Wallis, D. W., & Shepherd, A. (2009). Spatial and temporal evolution of Pine Island Glacier
503   thinning, 1995-2006. *Geophysical Research Letters, 36*, 5. Article. doi:L1750, 10.1029/2009gl039126
504 Wouters, B., Bamber, J. L., van den Broeke, M. R., Lenaerts, J. T. M., & Sasgen, I. (2013). Limits in detecting
505   acceleration of ice sheet mass loss due to climate variability. *Nature Geoscience, 6*(8), 613-616.
506   doi:10.1038/ngeo1874
507
508
509

510 References From the Supporting Information

511

512 Haran, T., Bohlander, J., Scambos, T., & Fahnestock, M. (2014, updated 2019). *MODIS mosaic of Antarctica 2008-
513   2009 (MOA2009) Image Map, Version 1*. doi:10.7265/N5KP8037
514 Howat, I. M. (2022). *The Reference Elevation Model of Antarctica – Mosaics, Version 2*.
515   doi:10.7910/DVN/EBW8UC
516 Rignot, E., Mouginot, J., & Scheuchl, B. (2017). *MEaSUREs InSAR-Based Antarctica Ice Velocity Map, Version 2*.
517   doi:10.5067/D7GK8F5J8M8R
518
519